ELSEVIER

Contents lists available at ScienceDirect

Computers and Geosciences

journal homepage: www.elsevier.com/locate/cageo





Cross-track infrared sounder cloud fraction retrieval using a deep neural network

Qian Liu a,b , Hui Xu c , Paul R. Houser b , Donglian Sun b , Matthew Rice b , Likun Wang c , Daniel Q. Duffy d , Chaowei Yang a,b,*

- ^a NSF Spatiotemporal Innovation Center, George Mason University, Fairfax, VA, 22030, USA
- b Department of Geography and GeoInformation Science, George Mason University, Fairfax, VA, 22030, USA
- Earth System Science Interdisciplinary Research Center, University of Maryland at College Park, College Park, MD, 20740, USA
- ^d NASA Center for Climate Simulation, Greenbelt, MD, 20771, USA

ARTICLE INFO

Keywords:
Cloud fraction
Hyperspectral infrared sounder
Deep neural network
CrIS
VIIRS

ABSTRACT

The retrieval of cloud fraction in satellite hyperspectral sounder field of view (FOV) is crucial for numerical weather prediction. This study proposes an innovative cloud fraction retrieval model for the hyperspectral infrared sounder - Cross-track Infrared Sounder (CrIS). The model is trained with a deep neural network (DNN), using the CrIS radiation spectra as the predictors and Visible Infrared Imaging Radiometer Suite (VIIRS) cloud mask as the learning target. An ensemble of randomly selected CrIS and VIIRS data are collocated and used as the training dataset. An optimized 5-layer neural network is built to establish the relationship between the CrIS spectra and the cloud fraction calculated from the VIIRS cloud mask within the CrIS FOV. In order to reduce the number of input predictors to enhance the efficiency of the model, a principal component transformation is performed on the original CrIS spectra and only the top 77 principal component scores are adopted as the final predictors. In general, the cloud fraction retrieved from the proposed DNN model are consistent with truth values calculated from the VIIRS cloud mask product. Further analysis on use cases demonstrates a slightly better cloud retrieval result during the daytime than that of the nighttime, and ocean retrievals are more accurate than land retrievals. However, since the relationship between CrIS spectrum and the cloud fraction is nonlinear, the model tends to slightly overestimate the cloud fractions over low cloud coverage regions and underestimate the values over high cloud fraction areas. Even so, the proposed model can still be a useful tool for obtaining cloud fraction information from hyperspectral infrared sounders and has the potential to be used for the numerical weather prediction and climate models, as well as other cloud studies.

1. Introduction

Clouds play a key role in the Earth's energy budget (Bretherton et al., 2005), the hydrological cycle (Sikma and Vilà-Guerau de Arellano, 2019) and the atmospheric circulation (Sherwood and Wahrlich, 1999). Clouds produce precipitation and regulate the balance of energy entering and leaving the climate system. Cloud fraction is defined as the proportion of cloud coverage in a satellite pixel or a weather or climate model grid box. It is one of the most crucial cloud parameters in modeling the downward radiation at both the Earth's surface and top of the atmosphere (Dürr and Philipona, 2004; Chen et al., 2012), and one of the largest sources of uncertainty in Global Climate Models (Mueller

et al., 2011; Wang et al., 2019). Since cloud fraction is a key factor in the climate models (Sekiguchi et al., 2003; Chuang et al., 2012; Liu et al., 2021), an accurate and reliable cloud coverage estimation is essential for climate studies.

Measurements from satellite infrared sounders provide valuable information for atmospheric profile retrievals, such as temperature, humidity, clouds, greenhouse gases, and so on. They are also directly assimilated into numerical weather prediction models (Jones et al., 2017; Li et al., 2016) and General Circulation models (Aumann et al., 2009) for weather forecasting, understanding the climate, and forecasting climate change. By design, the infrared sounders have a large footprint (greater than 10 KM in diameter), resulting in their fields of

E-mail address: cyang3@gmu.edu (C. Yang).

^{*} Corresponding author. NSF Spatiotemporal Innovation Center, George Mason University, 4400 University Dr., Exploratory Hall, Room 2211, Fairfax, VA, 22030, USA.

view (FOVs) often containing clouds, which can affect the atmospheric window channels. Many infrared sounder-based cloud cover retrieval algorithms have been developed for different purposes in the past two decades (McNally and Watts, 2003; Susskind et al., 2003; Smith and Taylor, 2004; Li et al., 2004; Eresmaa, 2013; Kahn et al., 2013; Wang et al., 2014; Lin et al., 2017; Liu et al., 2020). A widely used cloud cover retrieval method was developed by Susskind et al. (2003, 2006, 2011, 2014) for the Atmospheric Infrared Sounder (AIRS). In this retrieval method, the clear and cloudy observations are first identified using a cloud clearing method (Susskind et al., 2003). Later, the difference between the radiance of the satellite observations and that of selected channels in the model fit is used to estimate the effective cloud fraction. Assuming the cloud emissivity is spectrally flat, channels are selected that are most sensitive to clouds. This cloud cover retrieval method has been adopted in the AIRS cloud products (Kahn et al., 2013) and further extended to the Infrared Atmospheric Sounding Interferometer (IASI), as well as the Cross-track Infrared Sounder (CrIS) (Susskind et al., 2017; Christopher et al., 2021). It must be noted that the retrieved effective cloud fraction is the product of geometric fractional cloud cover and the cloud emissivity, rather than the real spatial cloud fraction within a sounder's FOV (Kahn et al., 2013), as it is difficult to accurately distinguish them using sounder measurements alone.

In addition to these approaches, the cloud coverage information of the hyperspectral infrared sounders can also be obtained from an accurate collocated imager. Li et al. (2004) developed an effective AIRS cloud detection method based on the cloud mask measured from Moderate Resolution Imaging Spectroradiometer (MODIS). In their study, each AIRS FOV is separately checked by its collocated MODIS cloud mask to determine whether it is cloudy or not. Similar methods also have been developed for the IASI (Eresmaa, 2013) and the CrIS (Wang et al., 2014, 2016) instruments. Since the sounder's cloud information is obtained from the high spatial resolution (usually around 1 km) imager, the sub-pixel, or partial cloud detection, as well as the cloud fraction retrieval for the infrared sounders becomes available. However, it usually takes a considerable amount of data, time, and computational resources to collocate the spatiotemporal data. To solve this issue, Liu et al. (2020) recently developed a novel CrIS cloud detection method based on the deep neural network (DNN). Deep neural network is one of the most widely used artificial intelligence (AI, Antun et al., 2020) and big data technologies (Yang et al., 2019) in the analytics of atmospheric phenomena (Liu et al., 2019; Schlef et al., 2019). Unlike the previous mentioned cloud-retrieval methods, the CrIS spectra are directly trained with VIIRS cloud mask for fast and accurate sounder cloud detection. After the DNN model is constructed, only the CrIS spectra is needed to determine its cloudy scene, avoiding the complex sounder-imager collocation pre-processing.

Even though promising results have been achieved when using the imager's information to identify infrared sounder's cloud contamination, most of these results have focused primarily on the cloud and clear sky differentiation. The imager's capability in checking sounder's subpixel cloud coverage has not been well discussed and explored. Since the advent of artificial intelligence (AI), researchers have been able to use machine and deep learning models to investigate complex phenomena in various scientific fields. As one of the most widely used AI models, deep neural network (DNN) can provide better solutions for problems with high-dimensional and non-linearity issues that usually have no direct analytically-derived solutions, such as the feature extraction for hyperspectral data (Li et al., 2019). As the microphysical and optical features of clouds are complex, it is hard to directly obtain the non-linearity relationship between infrared sounder observations and the cloud fractions using a physical model. Therefore, this paper innovatively develops a DNN model to automatically estimate the cloud fraction in hyperspectral infrared sounder FOV observations, using the CrIS instrument as an example, which provides a new insight for infrared sounder cloud fraction retrieval. The cloud mask of VIIRS, a high-resolution imager onboard the same satellite platform as CrIS, is

utilized as the truth to determine the cloud fraction in CrIS FOVs during the model training procedure. It is worth noting that the proposed method could be easily adopted by other hyperspectral infrared sounders. For example, AIRS could be trained using MODIS measurements, or IASI with Advanced Very-High-Resolution Radiometer (AVHRR). The results from this study can be further used in partial cloud detection and improving other cloud parameter retrievals as well as climate models.

The rest of the paper is organized as follows: Section 2 introduces the datasets used in this study; the methodology is summarized in Section 3; Section 4 presents a comprehensive evaluation on the performance of the cloud fraction retrieval model; and the discussion and conclusions are finally presented in section 5.

2. Data

2.1. Cross-track infrared sounder

The CrIS is a Fourier transform spectrometer onboard the Suomi National Polar-Orbiting Operational Environmental Satellite System (S-NPP) and Joint Polar Satellite System (JPSS-1) satellites, which has significantly enhanced performance over NOAA's legacy infrared sounder – the High Resolution Infrared Radiation Sounders (HIRS). The CrIS spectrum is measured in three infrared regions by a 3×3 gridded detector with a nadir resolution of 13.5 km: long-wave from 650 to $1095~{\rm cm}^{-1}$, middle-wave from 1210 to $1750~{\rm cm}^{-1}$, and short-wave from 2155 to 2550 cm $^{-1}$ (Han et al., 2013). The spectral information of CrIS channels is shown in Fig. 1.

2.2. Visible Infrared Imaging Radiometer Suite

The VIIRS, aboard the same platforms (S-NPP and JPSS-1) as CrIS, extends and improves upon a series of measurements initiated by certain legacy imagers, such as the AVHRR and MODIS. The VIIRS scans the earth spectrum in 22 radiance channels from visible (0.412 μm) to the thermal infrared (12.01 μm) bands (Cao et al., 2013), which includes 5 high spatial resolution bands (I-bands, 0.375 km at nadir), sixteen moderate spatial resolution bands (M-bands, 0.75 km at nadir), and one panchromatic day/night band (DNB, 0.75 km throughout the scan). In addition, it also provides various environmental products of the land, atmosphere, cryosphere, and ocean on a global scale with a higher spatial resolution and larger swath. As a key output from the VIIRS measurements, the VIIRS cloud mask (VCM) is now being widely used in different earth science studies.

3. Methodology

This study introduces a new CrIS cloud fraction retrieval method based on the DNN model. Fundamentally, the CrIS sub-pixel cloud

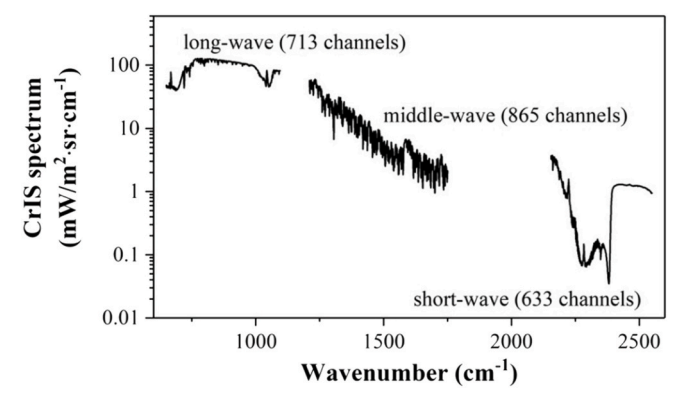


Fig. 1. Spectral information of CrIS channels.

information is trained from VIIRS, which requires the CrIS and VIIRS measurements to be collocated. Then, a series of hidden layers with different neurons is built to connect the collocated CrIS spectra and VIIRS cloud mask for CrIS cloud fraction retrieval. After the proposed model is built, the cloud fraction is directly predicted at each FOV with all the CrIS channel radiances. Details of each step are summarized as follows.

3.1. Cloud fraction determination

There are 34 field of regards (FOR) in one cross-track scanline, with 30 of them as Earth views, 2 of them as deep space views and the other 2 as instrument calibration views. In the normal spectral resolution (NSR) mode, the CrIS collects 1305 radiance channels with different spectral resolutions at the three infrared bands: 0.625 cm-1 in long-wave, 1.25 cm-1 in middle-wave, and 2.5 cm-1 in short-wave. The CrIS can also be operated in a full spectral resolution (FSR) mode. Under the FSR mode, the CrIS measures 2211 radiance channels over the three spectral regions with a spectral resolution of 0.625 cm-1 (Han and Chen, 2017). This study uses S-NPP CrIS FSR spectral information as the inputs and later performs a principal component (PC) transformation on the original radiances to reduce the number of predictors and thus improve model efficiency.

The VCM is determined by a series of strict checks (Kopp et al., 2014), with varying thresholds depending on different observational conditions. Its output has four flags, which are confidently clear, probably clear, probably cloudy, and confidently cloudy. The integer values assigned to these four types are 0, 4, 8 and 12, respectively. The VCM has a much finer spatial resolution than that of CrIS (0.75 km v.s 13.5 km), providing us with the opportunity to check CrIS's sub-pixel cloud coverage. In this study, the VCM is first collocated with CrIS FOV and then used to calculate the cloud fraction of CrIS which will be used as the learning target in the proposed model.

The key to this study is to build the relationship between CrIS spectra and the cloud fraction determined by the VIIRS cloud mask, which requires the collocation of the VIIRS cloud mask and the CrIS FOVs. The collocation is a time-consuming process, as it must search all the VIIRS pixels one-by-one at each CrIS FOV for accurate spatial and temporal collocation. Wang et al. (2016) developed an accurate collocation algorithm for CrIS and VIIRS based on their line-of-sight (LOS) pointing vectors at each CrIS FOV. Moreover, it uses a KD-tree searching strategy during the CrIS and VIIRS data pairing step, to reduces the collocation time. Previous research has confirmed that both CrIS and VIIRS are well-geolocation-calibrated instruments (Cao et al., 2013; Wang et al., 2013, 2017). Their collocation accuracy is at sub-pixel level with error less than 20 m (Wang et al., 2016). In this study, this collocation method is utilized to collocate CrIS spectra and the VIIRS cloud mask.

After CrIS is collocated with VIIRS, the VIIRS pixels within CrIS FOV are then adopted to calculate the cloud fraction of CrIS using equation (1),

$$CrIS_{(ef)} = \frac{N_{\left(Cloud,for\ VIIRS_{(VCM)} \ge 4\right)}}{N} \tag{1}$$

In equation (1), $CrIS_{(cf)}$ is the cloud fraction determined by the VIIRS cloud mask, $N_{(Cloud)}$ and N are the number of VIIRS cloudy pixels and total number of VIIRS pixels within CrIS FOV, respectively. Due to the geometric distortion caused by the scan mirror rotation, the total number of VIIRS pixels N in each CrIS FOV is not a constant. Instead, it changes with the scan mirror positions, ranging from around 200 to 1100 in every CrIS scanline. For the total number of cloudy scenes $N_{(Cloud)}$ determination, only confidently clear pixels are recognized as clear sky while the others are identified as cloudy in this study. Since VIIRS has a much finer spatial resolution than CrIS (which can be considered as a pure unit), the $CrIS_{(cf)}$ estimated from VIIRS provides accurate subpixel cloud information for CrIS.

Fig. 2 shows an example of the CrIS and VIIRS collocation and the cloud fraction determination process. As shown in Fig. 2a with the three VIIRS reflectance channels composited true color image (R: 0.672 μm, G: $0.555 \, \mu m$, B: $0.488 \, \mu m$) as the background, CrIS FOV footprint circled in orange is larger at the limb and smaller at the nadir positions, which requires the geometric distortion effect to be precisely considered during the collocation process. Fig. 2b shows the specific nine CrIS FOVs at the 17th FOR overlapping with the VIIRS true color image, and the corresponding collocated VIIRS cloud mask as well as the CrIS cloud fraction determined by equation (1) are presented in Fig. 2c and d, respectively. As clearly shown, only a portion of clouds enter the above three CrIS FOVs, while the other six CrIS FOVs are completely covered by the clouds. With assistance from the collocated high spatial resolution VIIRS, the CrIS cloud fraction information can be accurately estimated at every FOV. Fig. 2e shows the estimated cloud fraction for a whole CrIS scanline. As compared with Fig. 2a, the estimated CrIS cloud fraction is generally consistent with the cloud distributions shown in the VIIRS true color image.

3.2. DNN model building

After the CrIS cloud fraction is determined, the next step is to develop an accurate relationship between the CrIS spectra and the cloud fraction. To establish this connection, a data ensemble with sufficient samples is required. In order to include the general features and conditions of clouds, twelve days of the CrIS and VIIRS matched full orbit data pairs, covering every month (01/12, 02/07, 03/20, 04/03, 05/09, 06/27, 07/ 12, 08/16, 09/05, 10/22, 11/15, and 12/10) of 2018, are selected as the training dataset in this study. Moreover, to see if the selected training dataset is enough, a training dataset sensitivity test is performed by dividing the original twelve-day training dataset into two other training datasets, including a four-day dataset selected from different seasons (01/12, 04/03, 07/12, and 11/15 of 2018), and a six-day dataset selected every two months (01/12, 03/20, 05/09, 07/12, 09/05, 11/15 of 2018). Three different models are then generated with these training datasets and tested with the same independent dataset mentioned in section 3.4. Similar results are observed between these three training datasets trained models. The data sample change didn't bring significant improvement in the results, which implies that the training samples used in study are sufficient. In addition to the training dataset, an optimized 5-layer neural network, including one input layer which realize the principal component (PC) transformation, three fully connected hidden layers, and one output layer, is built to train the CrIS spectra for cloud fraction estimation. The VIIRS determined CrIS cloud fraction is used as the learning target for the training as well as the accuracy evaluation.

For the input layer, all the CrIS FSR 2211 channel radiances are used as the predictors. As the radiances measured from hyperspectral infrared sounders are highly correlated, a de-correlation needs to be performed on the original CrIS spectra before sending them to the hidden layers for the purpose of better regression, convergence, and faster prediction. As such, a PC transformation layer is added between the input and hidden layers, and the CrIS channel radiances are then converted into the PC scores $CrIS_{pcs}$ through equation (2) (Xu et al., 2018),

$$CrIS_{pcs} = \left(CrIS_{spec} - \overline{CrIS_{spec}}\right) \times N^{-1} \times E^{T}$$
(2)

where $CrIS_{spec}$ is the CrIS measured spectral radiances, $\overline{CrIS_{spec}}$ is the mean radiances of the CrIS channels of the training dataset and N is the instrument noises. E are the eigenvectors decomposed from equation (3) with the training dataset:

$$S = E \times \Lambda \times E^{T} \tag{3}$$

where S is the covariance matrix of the noise normalized radiances and Λ is the diagonal eigenvalue matrix. The symbol \times indicates matrix manipulation. By combining all the above matrices, equation (2) finally

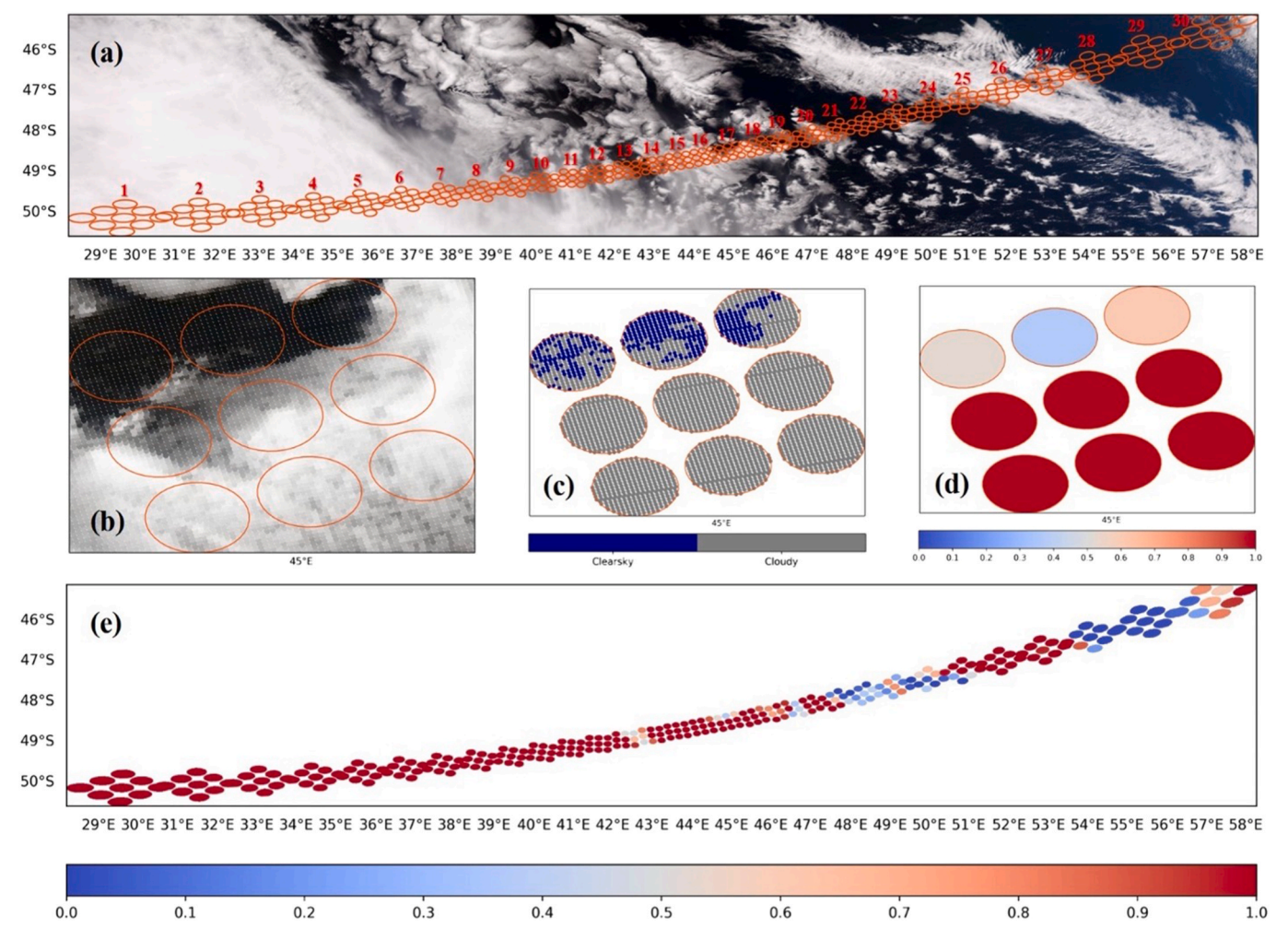


Fig. 2. Example of the spatiotemporal data collocation between CrIS and VIIRS on Mar. 10, 2019: (a) The true color image of VIIRS overlapping with the footprints (orange circle) of CrIS in one selected cross-track scanline. Numbers in (a) represent the CrIS FOR position; (b) same as (a) but for the 17th CrIS FOR; (c) the collocated VIIRS cloud mask within 17th CrIS FOR; (d) the cloud fraction of CrIS calculated from VIIRS cloud mask at the 17th FOR with values ranging from 0 (clear sky) to 1 (completely cloudy); (e) same as (d) but for a whole CrIS scanline. (For interpretation of the references to color in this figure legend, the reader is referred to the Web version of this article.)

becomes (4),

$$CrIS_{pcs} = CrIS_{spec} \times P_0 + W_0 \tag{4}$$

where P_0 is the PC transformation coefficients and W_0 is the channel dependent bias. The PC scores are a set of linearly uncorrelated new predictors that describe the same variances of the original dataset, and most of the effective Earth spectral variances are mainly distributed in the first few principal component scores. By only using the top k principal components as further predictors, one can greatly reduce the dimension and noise of the original inputs. Sensitivity tests and discussion for the selection of $CrIS_{pcs}$ are conducted in Section 3.3.

The hidden layer uses the PC scores as the inputs and further transforms them into the intermediate results for the output layer using the learnable parameters (weights and biases). Three fully connected hidden layers with 64, 128, and 32 neurons in each layer respectively are used in the DNN model to yield the most accurate prediction. Some general rules are followed in the selection of hidden layers and neurons. If the relationship between the predictors and the learning target are nonlinear and the training dataset has large dimensions, three to five hidden layers can be used to get an optimum solution. Therefore, three hidden layers were chosen to build the DNN model, as more hidden layers would also increase the complexity of the model and may potentially lead to overfitting. The number of hidden neurons is usually

set between the size of input layer and output layer. However, it can be more sometimes, which depends on use cases. In this study, the fixed values of 64, 128 and 32 neurons are used in the three hidden layers respectively, to capture the nonlinear relationship between CrIS spectrum and the cloud fraction. This may seem a little arbitrary but still in a reasonable neuron selection range.

All of the three hidden layers are activated with the Rectified Linear Unit (ReLU) activation function for non-linear training,

$$ReLU(x) = \begin{cases} 0, for \ x < 0 \\ x, for \ x \ge 0 \end{cases}$$
 (5)

where x in equation (5) is the input to a neuron. ReLU is a very simple function that returns the value directly if it is positive and otherwise returns zero. This activation function is considered a significant milestone in the field of deep learning and is proven to be an efficient way to develop very deep neutral networks (Agostinelli et al., 2014). The neurons within the hidden layers are used to calculate the weights and biases to minimize the difference between the prediction and the truth value through forward and backward propagations during the training process. The output layer is also activated with a ReLU function but was slightly modified, to correctly map the intermediate results produced by the last hidden layers to the final cloud fraction with values ranging from 0 to 1. The modified ReLU function $ReLU_{modified}$ is similar to the original

but restricts the value to 1 if the input is higher than 1, because a cloud fraction output higher than 1.0 is physically unreasonable.

Finally, a total of 3,663,777 CrIS and VIIRS paired data samples are selected as training data, with a third of them used to estimate model skill while tuning the hyperparameter. The final model evaluation is conducted using 1,242,720 independent data samples selected from different seasons. The model is developed using python 3.7 and tensorflow version 2.8. It is trained on a 64-bit Linux system server with 24 Intel(R) Xeon(R) CPUs running at 2.50 GHz. It usually takes 3-4 min to train one epoch, and the execution time of the learning procedure is around 2 days in total. It has to be noted that learning time can be greatly reduced if it is trained on a Graphical Processing Unit (GPU). While the prediction part is very fast after the model is successfully built, as only CrIS spectra is needed to estimate cloud fraction, avoiding the time intensive pre-processing steps. Using one-day CrIS data as an example, with approximately three million data samples in daytime and nighttime, the global cloud fraction information can be obtained within 10 min, demonstrating the model's strong capability in operational use.

Equation (6) shows how the cloud fraction value is estimated by the DNN model using CrIS FSR spectra,

3.3. Model optimization

The adaptive moment estimation (Adam) and batch gradient descent (BGD) searching strategy are adopted to optimize the loss function of the neural network during the model training procedure. As mentioned in section 3.2, the PC scores of the raw CrIS spectral data are calculated before being entered into the hidden layers, in order to optimize the model (e.g., de-correlation, dimensionality reduction, fast convergence and predication). A two-step sensitivity analysis is performed to determine the optimized PC predictors for the DNN model. Firstly, the model is trained and validated with different numbers of PC predictors ranging in increments of 10 from 10 to 150. As the 10-step sensitivity test line demonstrates in Fig. 4a, the best performing PC number producing the lowest mean square error (MSE), calculated from the differences of model predicted and the truth cloud fraction values of the training dataset based on one BGD iteration, falls between 60 and 90. After that, the model MSE shows a slightly increasing trend, which suggests that adding more PCs as model predictors would not improve the training accuracy. Based on the 10-step sensitivity test result (Fig. 4a), a further investigation is conducted by changing the PC numbers from 60 to 90

$$CrIS_{cf} = ReLU_{modified}(ReLU(ReLU(ReLU(CrIS_{spec} \times P_0 + W_0) \times P_1 + W_1) \times P_2 + W_2)) \times P_3 + W_3) \times P_4 + W_4)$$
(6)

In equation (6), a CrIS spectrum $CrIS_{spec}$ is first converted to its $CrIS_{pcs}$ with P_0 and W_0 . Then the $CrIS_{pcs}$ is further transformed to the intermediate results through three ReLU activated hidden layers using the model trained coefficients P_1, P_2, P_3 and W_1, W_2, W_3 . The outputs from last hidden layer are finally converted to the cloud fraction using P_4 and W_4 and the modified ReLU. All model coefficients are determined by the training dataset during the training process. The proposed CrIS cloud fraction retrieval framework is illustrated in Fig. 3. The implemented code of the DNN model is shared in GitHub with a detailed README file to describe the whole procedure: https://github.com/qian9834/Cloud-fraction-retrieval.

Input data collocation

with a 1-step equal interval, to find the final PC predictors for the DNN model (Fig. 4b). Due to the stochastic characteristic of deep learning models, the optimized PC number with lowest MSE varies slightly in different set of training experiments even with the exact same parameters. Therefore, the sensitivity test repeats the second step 20 times (blue dish lines in Fig. 4b) and uses their mean value (black solid lines in Fig. 4 (b)) to determine the best number of PC predictors. As the results show, a PC number of 77 produces the lowest MSE on average. Therefore, this study cuts off the CrIS principal component scores at 77 (red arrow line in Fig. 4b), and only the top 77 *CrIS*_{pcs} are used as the final predictors of the DNN model.

The DNN model is then trained with the selected PC predictors on a series of epochs until the MSE levels off, after the lowest point of MSE. To achieve this goal, this study adopts an adaptive learning rate strategy. Using 100 epochs as a training group, the model yielding the lowest MSE

Retrieval result

Input layer PC layer 77 PCs, t observations RELU: $f(x) = \begin{cases} 0, for \ x < 0 \\ x, for \ x \ge 0 \end{cases}$ Cloud fraction RELU: $f(x) = \begin{cases} 0, for \ x < 0 \\ x, for \ x \ge 0 \end{cases}$ Unique layer Cloud fraction RELU: $f(x) = \begin{cases} 0, for \ x < 0 \\ x, for \ x \ge 0 \end{cases}$ The proof of th

Forward propagation (prediction)

Backward propagation (learning)

Fig. 3. Flow chart of CrIS cloud fraction retrieval framework based on DNN model.

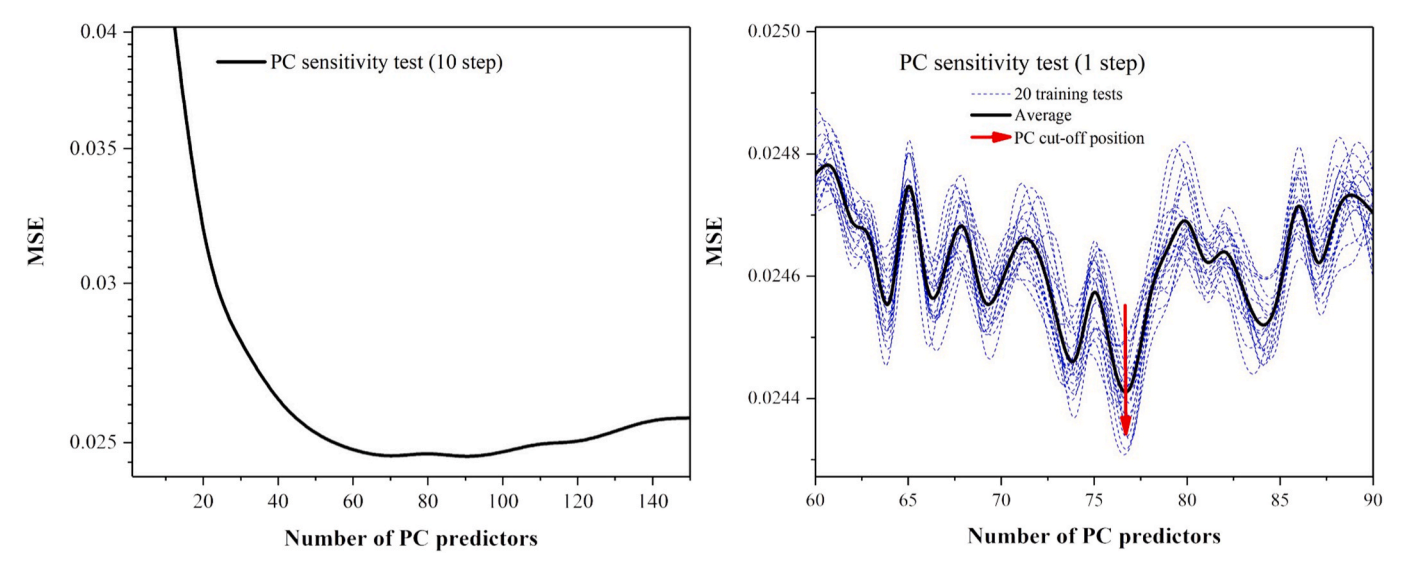


Fig. 4. Sensitivity test result on the input PC number. (a) 10-step (b) 1-step.

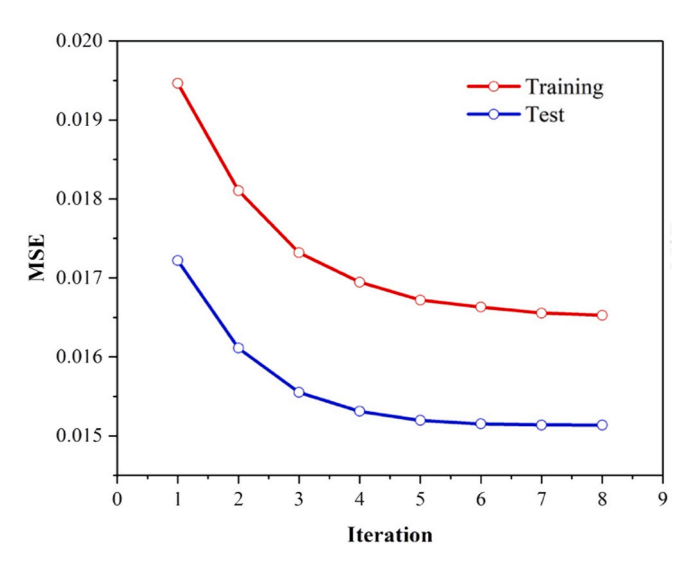


Fig. 5. The lowest model MSE per training group on the training and validation datasets.

within the group is chosen. After one training group is finished, the model is further trained based on the best result (lowest MSE) of the last training group, with an adjusted learning rate decayed by half of the previous one. The training procedure is finally terminated when the MSE of the validation plateaus. The choice of the starting learning rate is arbitrary. In this study, it is set as 0.001 at the beginning. Fig. 5 shows the lowest model MSE as a function of the training group on the training data (red line) and validation (blue line) data separately. As clearly shown, the training MSE keeps decreasing as more training is conducted. However, the validation MSE stays relatively consistent after 6th training group. This suggests that the model may have learned the training dataset after the 6th training group, and additional training has no significant improvement upon the validation dataset. It is therefore unnecessary to conduct more training after this point. In addition, it is reasonable to see a lower validation MSE as compared with the training result, since the model uses a dropout regularization (the neuron dropout rate is 5%) at each hidden layer to avoid potential over-fitting. The dropout is only activated during the training phase but deactivated when evaluating on the validation data, resulting in a better function in the latter case. Finally, the model is determined at the 60th epoch of the 8th training group which yields the lowest validation MSE of 0.0152 among all of the total 800 training epochs.

3.4. Model accuracy analysis

The accuracy of the proposed DNN model is analyzed based on a test (or holdout) dataset with 1,242,720 data samples in total selected from four different seasons of Feb. 15, May 15, Jul. 10 and Nov. 10 of 2018. The test data for this accuracy analysis is different from the validation data mentioned in previous sections. It is an independent dataset which has not been used during the model training, and it can thus produce an unbiased estimate of final DNN model's performance. In addition to the MSE discussed at the training stage, the Pearson's correlation coefficient (R) is also adopted as a metric to evaluate the model accuracy by measuring the correlation between the model prediction and truth.

As shown in Fig. 6, the predicted CrIS cloud fraction is mostly distributed near the 1:1 diagonal line (black dish line) with high probability density. The fitting line (solid red line) with a slope of 1.002 and very tiny bias of 0.007, nearly overlaps the diagonal line, indicating a very solid correlation between the model prediction and truth. Additionally, the reliable performance of the DNN model can be illustrated with its low MSE of 0.021 and high R value of 0.924. As compared with Fig. 6, the MSE calculated from the test data is only slightly higher than that calculated from both the training and validation data during the training process, indicating that the model is well trained with neither significant under-fitting nor over-fitting.

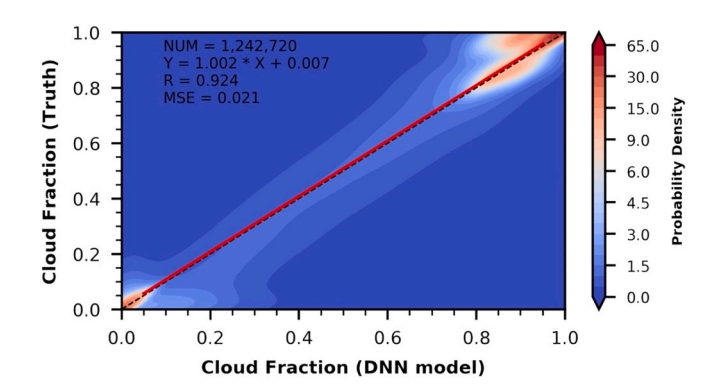


Fig. 6. Probability density plot of the DNN model predicted and truth cloud fractions. The red solid line and black dish line are the fitting line and 1:1 diagonal line, respectively. (For interpretation of the references to color in this figure legend, the reader is referred to the Web version of this article.)

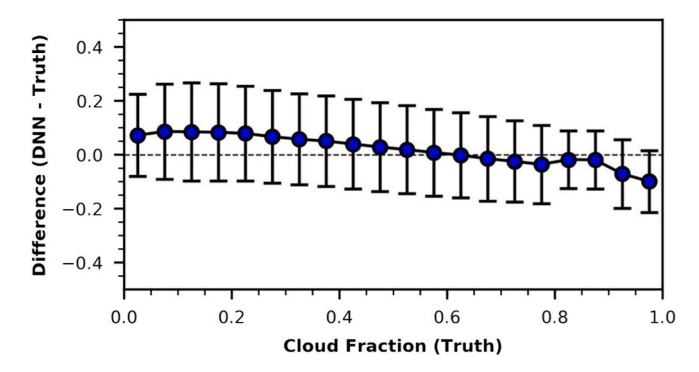


Fig. 7. Distribution of difference between predicted and truth cloud fractions as a function of cloud fraction. Blue dot and error bar indicates the mean bias and standard deviation of the difference in the corresponding interval (0.05), respectively. (For interpretation of the references to color in this figure legend, the reader is referred to the Web version of this article.)

Fig. 7 shows the differences between DNN predicted cloud fraction and the truth cloud fraction. The blue dot and vertical error bar represent the mean and standard deviation of their differences in the corresponding bins (the bin size is 0.05), respectively. As shown, the 1-sigma uncertainty at each bin is not identical, ranging from 0.108 to 0.182. The uncertainty in the low cloud fraction regions (partially thin cloudy scenes) is overall slightly higher than that in the high cloud fraction, where the scenes are almost fully covered by clouds. This is because the spectral features of thin cloud and clear sky are very similar to each other. Moreover, the mixed strong surface signals can increase the complexity of the spectra observed in the thin partially cloudy scenes, which may result in a higher retrieval uncertainty in these areas. Another result that can be identified from Fig. 7 is that the DNN model tends to overestimate the cloud fraction with values less than 0.5, especially for those very thin partially cloudy scenes. The average overestimation is around 0.078 for cloud fraction less than 0.1. On the other hand, cloud fraction with values over 0.5 are likely to be underestimated. The largest negative difference between model predictions and the truth values are located near 1.0 with an average underestimation of 0.085. The main explanation for this is that the relationship between CrIS spectra and the cloud fraction is nonlinear, which results in the predictions from the DNN model systematically overestimating the actual values for one range and underestimating them for another. Another possible reason for the underestimation is that the modified ReLU function in the output layer forces all the output to be smaller than or equal to 1.0, so that some potential overestimation results have been eliminated. We should also be aware that cutting off PCs may potentially reduce the model accuracy, because the abandoned PCs may also contain some cloud fraction related information. However, considering the effectiveness of PCA on reducing the data complexity of hyperspectral infrared sounders, conducting PC transformation is worthwhile as it indeed optimizes the model inputs. Nevertheless, the predictions agree well with the considered truth values with a high correlation coefficient of 0.924, as shown in Fig. 5.

4. Use case study

The performance of the proposed cloud fraction retrieval model is investigated on a series of independent use cases selected from 2018 to 2019, all of which are excluded from the training dataset to prevent bias in error estimates.

4.1. Oct. 30, 2018

Fig. 8 shows the daytime global cloud distribution maps of Oct. 30, 2018. As presented in the VIIRS true color image (Fig. 8a), more than 60% of the global land and ocean areas are covered by clouds. This can

also be identified in Fig. 8b, the truth CrIS cloud fraction map, that was determined by the VIIRS cloud mask. The purely clear sky and partially thin cloudy scenes (blue areas with cloud fraction less than 0.2) are mainly located over the land part of the coastal areas of United States, southern Argentina, Sahara Desert, southern Africa, southwest Asia, north India, northwest China, and large portions of Australia and Antarctica. Given the retrieval results produced by the proposed DNN model (shown in Fig. 8c) compared to that of Fig. 8b, the DNN model accurately predicts the majority of the cloud fraction. Their difference map shown in Fig. 8d further confirms that the cloud fraction retrieved from the DNN model agree well with the truth values on a global scale. However, relatively larger difference values are observed over the partially thin cloudy areas. As mentioned, this is possibly due to the strong surface signals, which makes it hard for the model to correctly classify thin clouds. In addition, as clearly shown in Fig. 8e, the MSE in high latitude regions (greater than $\pm 60^{\circ}$) are larger than that in the low latitude regions. This may be attributed to the relatively low accuracy of cloud mask product of VIIRS (which is adopted as the learning target) over high latitude areas, which are ~88% in snow covered land and 72% in Antarctic and Greenland (Zhou et al., 2019). The inaccurate inputs from VIIRS in these scenarios will introduce inaccuracy to the model during training, thus reducing the model's ability to correctly estimate cloud fraction over these areas. In addition, both VIIRS and CrIS have larger instrument noises over the cold scenes, which may also reduce the accuracy over the high latitude regions. Fig. 8f shows the histogram of the differences between the model prediction and truth. As shown, their residuals are almost uniformly distributed around the zero line, with a mean of -0.007 and standard deviation of 0.134, and most of them are less than 0.2 (~91%) and 0.1 (~74%). The quantitative relationship between the model predictions and truth is illustrated in Fig. 8g. A favorable correlation of 0.929 between the CrIS predicted and VIIRS determined cloud fraction is obtained for this particular case. The daytime MSE is 0.018, which is slightly lower than that of the model value as discussed in section 3.4. All these statistics demonstrate that the proposed DNN model works very well for the daytime cloud fraction retrievals.

The investigation on the model nighttime performance is also conducted in this study, and the results are presented in Fig. 9. Since the reflectance channels are not available at night, the VIIRS moderate resolution band 14 (M14 at $8.55 \mu m$) brightness temperature is used as the reference image (Fig. 9a) for this discussion. Essentially, the lower the brightness temperature, the more likely the scene is contaminated by clouds, especially over low latitude regions, such as those in tropical areas which might be covered by deep convective clouds. As indicated by the truth CrIS cloud fraction in Fig. 9b and compared with the model prediction in Fig. 9c, it is encouraging to see that the results retrieved from the DNN model are consistent with the truth values over nighttime observations. Similar to the daytime case, their larger differences are mainly observed over the poles and other snow-covered regions (as shown in Fig. 9d and e), partially due to the relatively poor performance of VIIRS cloud mask. Specifically, for those of the low latitude areas, the model MSE is quite small and mostly distributed between 0.01 and 0.02. However, the MSE values in high latitude areas are much higher, with the maximum values (\sim 0.08) at around \pm 80°. This suggests that the model performance is reduced over the high latitude areas, and it should be used with caution in these regions. The statistical result in Fig. 9f show a tiny negative bias of -0.013, suggesting that the nighttime retrieval result is slightly underestimated. This can also be identified from the positive offset of the fitting line (solid red line) shown in Fig. 9g. The standard deviation is 0.151 also implies that the overall uncertainty of the nighttime retrieval results is slightly higher than that of the daytime (0.134). Regardless, the metrics shown in Fig. 9g still suggest a high similarity between the model predictions and truth. According to the colored probability density plot, the fitting line is nearly coincident with the 1:1 line, revealing a relatively accurate estimation from the DNN model as compared with truth. The low MSE (0.023) and

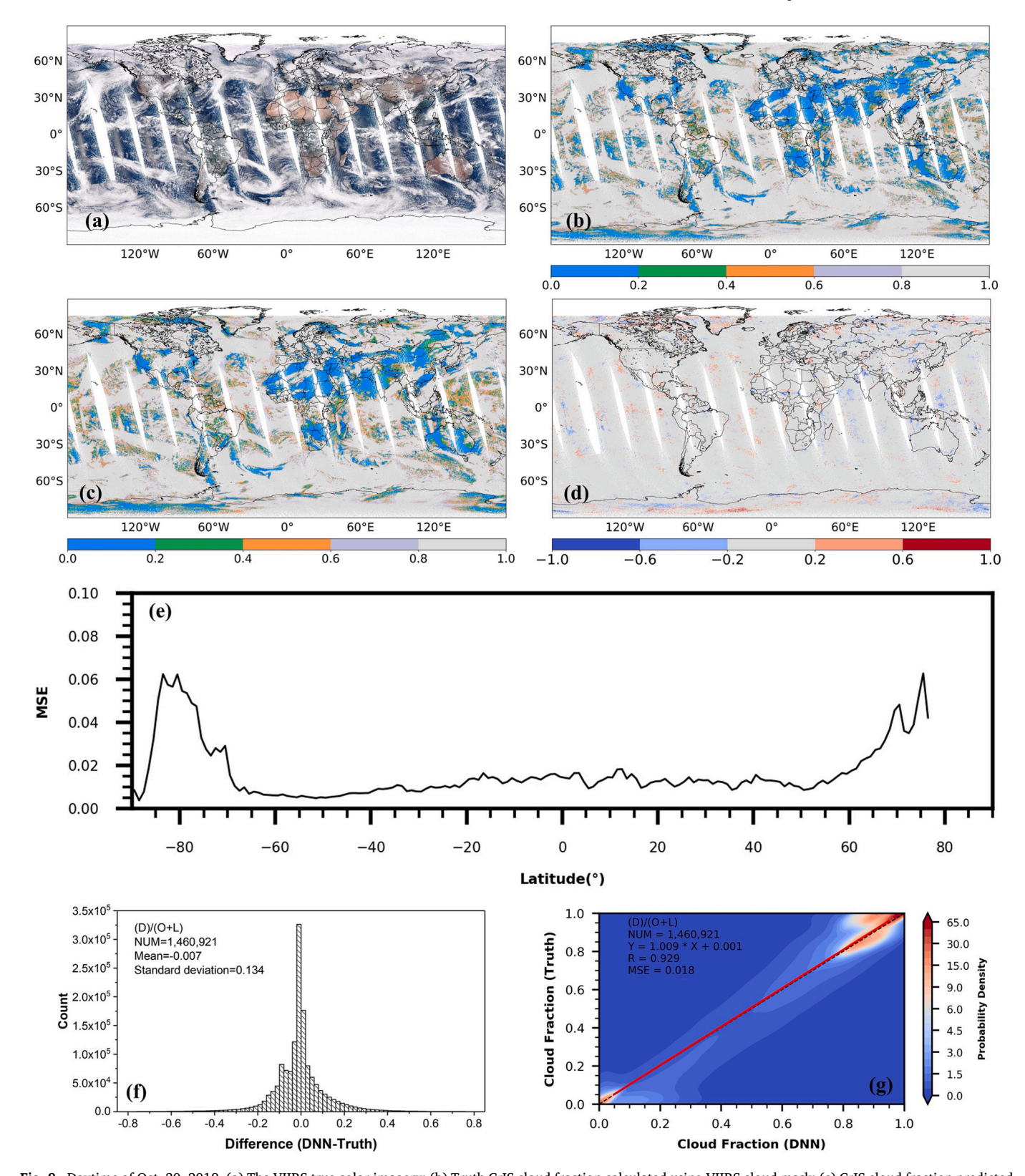


Fig. 8. Daytime of Oct. 30, 2018. (a) The VIIRS true color imagery; (b) Truth CrIS cloud fraction calculated using VIIRS cloud mask; (c) CrIS cloud fraction predicted by the proposed model; (d) Difference between (c) and (b); (e) The model MSE distribution over different latitude; (f) the histogram of (d); (g) Probability density plot of the model prediction and truth. The "D/O + L" in (f) and (g) represents all of the daytime (D) ocean (O) and land (L) data. The red solid line and black dish line in (g) are the fitting line and 1:1 diagonal line. (For interpretation of the references to color in this figure legend, the reader is referred to the Web version of this article.)

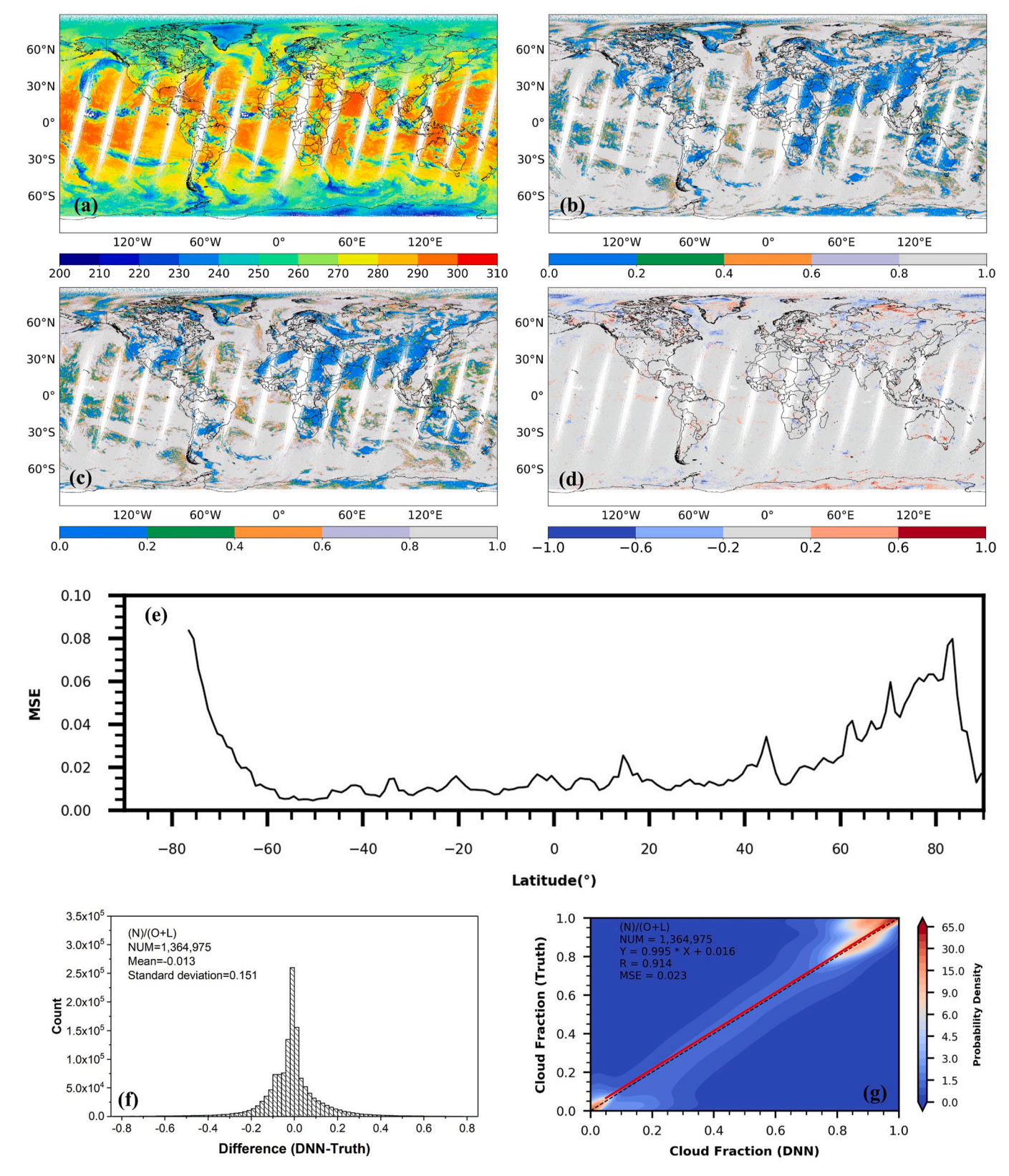


Fig. 9. Same as Fig. 8 but for the nighttime of Oct. 30, 2018. Particularly, the VIIRS M14 brightness temperature is used as the reference image in (a) instead of the true color image, as the reflectance channels are not available at night. The "N/O + L" in (f) and (g) represents all of the nighttime (N) ocean (O) and land (L) data. (For interpretation of the references to color in this figure legend, the reader is referred to the Web version of this article.)

Table 1Test metrics of the model accuracy on Oct. 30, 2018.

Date	Metrics	Daytime			Nighttime			Total
		Land	Ocean	Globe	Land	Ocean	Globe	
10/30/2018	MSE R	0.029 0.908	0.011 0.944	0.018 0.929	0.035 0.896	0.018 0.916	0.023 0.914	0.020 0.922

high R (0.914) further confirms that the model performs very well for nighttime observations.

Table 1 presents detailed quantitative comparisons between results calculated from the daytime and nighttime data. In general, the DNN model achieves a higher accuracy over daytime than nighttime, with a lower MSE (0.018 vs 0.023) and higher R (0.929 vs 0.914). The lower accuracy observed in the nighttime case is likely due to the weaker signal received by CrIS at nighttime, which makes the spectral contrast among FOVs much smaller. A similar mechanism can occur in the VIIRS instrument, leading to a relatively lower accuracy of the nighttime cloud mask as well as truth cloud fraction. Furthermore, the model tends to exhibit better performance over the ocean than the land areas. The averaged (day and night) MSE and correlation coefficient over ocean are 0.015 and 0.930, respectively, while over land they are 0.032 and 0.902, respectively. The main explanation for this is that the surface cover over land is more heterogenous than that of the ocean, which increases the complexity of the satellite observed spectra over land. In addition, the mixed-pixel issue (inhomogeneous scene) over land also increases the difficulty of accurate cloud identification.

4.2. Other cases

One week of the global CrIS and VIIRS data selected from Jun 1 to Jun. 7, 2020, are further analyzed in the following study, to evaluate the robust performance of the DNN model, with results summarized in Table 2.

The accuracy metrics shown in Table 2 demonstrate that the proposed cloud fraction retrieval model produces reliable and robust predictions for a continuous seven days. For the daytime, the model MSE has little fluctuation, with values ranging from 0.015 to 0.018 over land, and from 0.012 to 0.014 over ocean in this one-week analysis. The cloud fraction correlation coefficient between DNN model predictions and the truth values is relatively high and stable for all the daytime cases, averaging 0.944. The model MSE at nighttime has a slightly larger variation than the daytime MSE, fluctuating between 0.040 and 0.053 over land, and between 0.019 and 0.023 over ocean. The mean correlation coefficient at nighttime is 0.904 with values ranging from 0.889 to 0.913. Overall, the global (all ocean, land, daytime, and nighttime)

mean MSE and correlation coefficient are 0.021 and 0.922 respectively for these selected continuous use cases, which are comparable to the model metrics (0.021 and 0.924) as discussed in the previous section. All tests demonstrate the stability of the DNN model and illustrate its potential to be an effective tool for cloud fraction retrieval.

Even though the seasonal impacts have been considered in the training dataset selection, it is still worthwhile to determine whether the seasonal change impacts the cloud fraction retrieval result. Table 3 shows the accuracy metrics calculated with the data randomly selected from different seasons of Feb. 15, 2018, May. 15, 2018, Jun. 10, 2018, and Nov. 10, 2018. The results show that the model overall accuracy has a small variation, with MSE ranging from 0.020 to 0.022 and the Pearson's r from 0.921 to 0.931 in different seasons. These tests demonstrate that the DNN model overall is stable and the seasonal impact in general is small.

5. Discussion and conclusion

While cloud fraction information is critical for climate models as well as various meteorological applications, an efficient cloud fraction retrieval method is still needed. We propose a novel cloud fraction retrieval framework by leveraging the state-to-art AI deep neural network models, to estimate the cloud fraction within a single FOV of the infrared hyperspectral sounder (CrIS) at high efficiency and automation. Through analysis of model performance on a test dataset covering all seasonal conditions and several other individual use cases, the proposed model is proven to accurately retrieve cloud fraction under different spatiotemporal domains.

In general, the model achieves a high cloud fraction retrieval accuracy, with a low MSE of 0.02 and high R of 0.924, as compared with the truth calculated from the VIIRS cloud mask. Moreover, the model tends to have better results during daytime than nighttime with MSE values of 0.014 vs 0.030. The better performance in the daytime is because the signal received by the instrument in the daytime is much stronger than that of the nighttime, enabling both the CrIS and VIIRS to capture more information of the clear sky as well as cloud features, and thus making their spectra much easier to be distinguished during the daytime. Furthermore, the model performs better over ocean than land with MSE

Table 2Test metrics of the model accuracy from Jun. 01, 2020 to Jun. 07, 2020.

Date	Metrics	Daytime			Nighttime			Total
		Land	Ocean	Globe	Land	Ocean	Globe	
06/01/2020	MSE	0.015	0.014	0.014	0.044	0.023	0.030	0.022
	R	0.951	0.934	0.944	0.875	0.902	0.897	0.920
06/02/2020	MSE	0.016	0.014	0.014	0.052	0.022	0.033	0.023
	R	0.949	0.930	0.942	0.842	0.905	0.889	0.915
06/03/2020	MSE	0.017	0.013	0.014	0.048	0.019	0.029	0.021
	R	0.944	0.935	0.943	0.854	0.918	0.902	0.923
06/04/2020	MSE	0.017	0.012	0.014	0.04	0.019	0.025	0.019
	R	0.943	0.937	0.944	0.881	0.921	0.913	0.929
06/05/2020	MSE	0.018	0.013	0.014	0.050	0.019	0.029	0.021
	R	0.943	0.938	0.945	0.851	0.921	0.900	0.922
06/06/2020	MSE	0.016	0.013	0.014	0.048	0.019	0.029	0.021
	R	0.950	0.937	0.946	0.861	0.921	0.903	0.924
06/07/2020	MSE	0.017	0.013	0.014	0.053	0.019	0.030	0.022
	R	0.947	0.937	0.945	0.844	0.924	0.900	0.922
Mean	MSE	0.017	0.013	0.014	0.048	0.020	0.030	0.021
	R	0.946	0.936	0.944	0.858	0.915	0.904	0.922

Table 3 Test metrics of the model accuracy for data selected from different seasons.

Date	Metrics	Daytime			Nighttime			Total
		Land	Ocean	Globe	Land	Ocean	Globe	
02/15/2018	MSE	0.030	0.015	0.021	0.042	0.014	0.023	0.022
	R	0.906	0.925	0.921	0.878	0.943	0.925	0.923
05/15/2018	MSE	0.018	0.013	0.015	0.047	0.021	0.031	0.022
	R	0.943	0.935	0.944	0.863	0.907	0.898	0.921
07/10/2018	MSE	0.014	0.015	0.015	0.034	0.021	0.025	0.020
	R	0.958	0.927	0.945	0.903	0.904	0.916	0.931
11/10/2018	MSE	0.027	0.011	0.017	0.039	0.016	0.022	0.020
	R	0.909	0.940	0.927	0.883	0.933	0.922	0.925

values of 0.017 vs 0.033, which can be attributed to simpler surface coverage and less signal disturbance from the surrounding environment. The DNN model overestimates the cloud fraction over areas with low cloud coverage and underestimates those over areas with high cloud coverage. This is because the relationship between the model predictors (CrIS spectra) and the cloud fraction values is nonlinear. In addition, larger uncertainty is observed over thin cloudy areas, possibly because the spectra of clear sky and thin cloud are similar with each other, making it hard for the model to correctly predict these two scenarios. Moreover, a lower model accuracy is also observed over high-latitude regions covered by snow or ice. The main explanation for this is that the accuracy of VIIRS cloud mask is relatively low over these areas, therefore, reducing the model's ability to retrieve cloud fraction over

Following the work presented in this paper, future work will focus on improving the following aspects to increase the model's performance:

- 1) Improving the training dataset. The CrIS and VIIRS data has recently been reprocessed with optimal algorithms through their life cycle (Zou et al., 2020; Chen et al., 2021), and the accuracies of both have been improved. Therefore, the model will be retrained with updated data soon to see if its performance can be further improved.
- 2) Improving the model. First, more sensitivity tests will be conducted to tune the parameters and optimize the model, such as the use of a more complex neural network during training or different combinations of neurons, PC numbers and epochs. Additionally, the model will be trained under different situations so that the model performance will be improved over low accuracy areas. This can be achieved, for example, by training the model for land, ocean, daytime, and nighttime scenarios separately.

Lastly, the methodology described in this study can be easily adapted to other similar instruments, such as AIRS and IASI. Additionally, this methodology can be utilized for other non-hyperspectral satellite instrument pairs as well, provided that the lower and higher spatial resolution instruments could be accurately collocated together in a similar way as described in this paper. The retrieval model detailed in this paper can be particularly useful in partial cloud detection. Currently, the infrared sounder data serving in NWPs and GCMs can be classified as clear sky or cloudy, whereas partially cloudy scenes are undeterminable. However, this information is crucial for climate models, as the influence of partially cloudy scenes produces very different radiative forcing effects of the atmosphere than that of the scenes covered by cloud entirely. Further investigation of the partial cloud detection method could promote the application of the proposed cloud retrieval methodology in an operational mode for various applications, such as big spatiotemporal remote sensing data analytics and prediction accuracies improvement for GCMs and NWPs.

6. Computer code availability

Our cloud-fraction-retrieval model training and testing codes, and trained cloud-fraction-retrieval model for CrIS are available in a GitHub

repository at: https://github.com/qian9834/Cloud-fraction-retrieval.

CRediT authorship contribution statement

Qian Liu: Writing - original draft, model development, trained the model and drafted the manuscript. Hui Xu: Writing - original draft, model development. Paul R. Houser: draft and review the manuscript, Donglian Sun: draft and review the manuscript, Matthew Rice: draft and review the manuscript, Likun Wang: collocation method providing. Daniel Q. Duffy: acquired funding. Chaowei Yang: Supervision, Funding acquisition, acquired funding, and method discussion and manuscript review and revision. All authors have read, reviewed, and approved the manuscript.

Declaration of competing interest

The authors declare that they have no known competing financial interests or personal relationships that could have appeared to influence the work reported in this paper.

Data availability

all data are shared through the website.

Acknowledgements

The CrIS and VIIRS data used in this study are downloaded from NOAA/Comprehensive Large Array Data Stewardship System (CLASS). Research is funded by NASA (80NSSC19P2033) and NSF (CNS 1841520 and ACI 1835507).

7. Abbreviations

AI	Artificial Intelligence
AIRS	Atmospheric Infrared Sounder
AVHRR	Advanced Very-High-Resolution Radiometer
CrIS	Cross-track Infrared Sounder
DNB	Day/Night Band
DNN	Deep neural network
FOR	Field of Regards
FOV	Field of View
FSR	Full Spectral Resolution
HIRS	High Resolution Infrared Radiation Sounders
IASI	Infrared Atmospheric Sounding Interferometer
JPSS-1	Joint Polar Satellite System
LOS	Line of Sight
MODIS	Moderate Resolution Imaging Spectroradiometer
NSR	Normal Spectral Resolution
PC	Principal Component
ReLU	Rectified Linear Unit
S-NPP	Suomi National Polar-Orbiting Operational Environmental

Satellite System

11

VCM VIIRS Cloud Mask

VIIRS Visible Infrared Imaging Radiometer Suite

References

- Agostinelli, F., Hoffman, M., Sadowski, P., Baldi, P., 2014. Learning Activation Functions to Improve Deep Neural Networks arXiv preprint arXiv:1412.6830.
- Antun, V., Renna, F., Poon, C., Adcock, B., Hansen, A.C., 2020. On instabilities of deep learning in image reconstruction and the potential costs of AI. Proc. Natl. Acad. Sci. USA 117 (48), 30088–30095.
- Aumann, H.H., Manning, E., Barnet, C., Maddy, E., Blackwell, W., 2009. An anomaly correlation skill score for the evaluation of the performance of hyperspectral infrared sounders. In: Atmospheric and Environmental Remote Sensing Data Processing and Utilization V: Readiness for GEOSS III, vol. 7456. International Society for Optics and Photonics, 74560T. August.
- Bretherton, C.S., Blossey, P.N., Khairoutdinov, M., 2005. An energy-balance analysis of deep convective self-aggregation above uniform SST. J. Atmos. Sci. 62 (12), 4273–4292.
- Cao, C.Y., Xiong, J., Blonski, S., Liu, Q.H., Uprety, S., Shao, X., Bai, Y., Weng, F.Z., 2013. Suomi NPP VIIRS sensor data record verification, validation, and long-term performance monitoring, J. Geophys. Res. Atmos. 118 (22), 11664–11678.
- Chen, L., Yan, G., Wang, T., Ren, H., Calbó, J., Zhao, J., McKenzie, R., 2012. Estimation of surface shortwave radiation components under all sky conditions: modeling and sensitivity analysis. Remote Sens. Environ. 123, 457–469.
- Chen, Y., Iturbide-Sanchez, F., Tremblay, D., Tobin, D., Strow, L., Wang, L., Mooney, D. L., Johnson, D., Predina, J., Suwinski, L., Revercomb, H.E., 2021. Reprocessing of Suomi NPP CrlS sensor data records to improve the radiometric and spectral long-term accuracy and stability. IEEE Trans. Geosci. Rem. Sens. 60, 1–14.
- Christopher, D.B., Divakarla, M., Gambacorta, A., Iturbide-Sanchez, F., Nalli, N.R., Pryor, K., Tan, C., Wang, T., Warner, J., Zhang, X., Zhu, T., 2021. NOAA unique combined atmospheric processing system (NUCAPS) algorithm theoretical basis document. Version 3.0 Available at: https://www.star.nesdis.noaa.gov/jpss/documents/ATBD/ATBD_NUCAPS_v3.1.pdf. (Accessed June 2021).
- Chuang, C.C., Kelly, J.T., Boyle, J.S., Xie, S., 2012. Sensitivity of aerosol indirect effects to cloud nucleation and autoconversion parameterizations in short-range weather forecasts during the May 2003 aerosol IOP. J. Adv. Model. Earth Syst. 4, M09001.
- Dürr, B., Philipona, R., 2004. Automatic cloud amount detection by surface longwave downward radiation measurements. J. Geophys. Res. Atmos. 109 (D5).
- Eresmaa, Reima, 2013. Imager-assisted cloud detection for assimilation of infrared atmospheric sounding interferometer radiances. Q. J. R. Meteorol. Soc. 140, 2342–2352
- Han, Y., Chen, Y., 2017. Calibration algorithm for cross-track infrared sounder full spectral resolution measurements. IEEE Trans. Geosci. Rem. Sens. 56 (2), 1008–1016.
- Han, Y., Revercomb, H., Cromp, M., Gu, D., Johnson, D., Mooney, D., Scott, D., Strow, L., Bingham, G., Borg, L., Chen, Y., 2013. Suomi NPP CrlS measurements, sensor data record algorithm, calibration and validation activities, and record data quality. J. Geophys. Res. Atmos. 118 (22), 12–734.
- Jones, T.A., Koch, S., Li, Z., 2017. Assimilating synthetic hyperspectral sounder temperature and humidity retrievals to improve severe weather forecasts. Atmos. Res. 186, 9–25.
- Kahn, B.H., Irion, F.W., Dang, V.T., Manning, E.M., Nasiri, S.L., Naud, C.M., Blaisdell, J. M., Schreier, M.M., Yue, Q., Bowman, K.W., Fetzer, E.J., 2013. The atmospheric infrared sounder version 6 cloud products. Atmos. Chem. Phys. 13, 14477–14543.
- Kopp, T.J., Thomas, W., Heidinger, A.K., Botambekov, D., Frey, R.A., Hutchison, K.D., Iisager, B.D., Brueske, K., Reed, B., 2014. The VIIRS Cloud Mask: progress in the first year of S-NPP toward a common cloud detection scheme. J. Geophys. Res. Atmos. 119 (5), 2441–2456.
- Li, J., Menzel, W.P., Sun, F., Schmit, T.J., Gurka, J., 2004. AIRS subpixel cloud characterization using MODIS cloud products. J. Appl. Meteorol. 43 (8), 1083–1094.
- Li, J., Wang, P., Han, H., Li, J., Zheng, J., 2016. On the assimilation of satellite sounder data in cloudy skies in numerical weather prediction models. J. Meteorol. Res. 30 (2), 169–182.
- Li, S., Song, W., Fang, L., Chen, Y., Ghamisi, P., Benediktson, J.A., 2019. Deep learning for hyperspectral image classification: an overview. IEEE Trans. Geosci. Rem. Sens. 57 (9), 6690–6709.
- Lin, L., Zou, X., Weng, F., 2017. Combining CrIS double CO2 bands for detecting clouds located in different layers of the atmosphere. J. Geophys. Res. Atmos. 122 (3), 1811–1827.

- Liu, Q., Li, Y., Yu, M., Chiu, L.S., Hao, X., Duffy, D.Q., Yang, C., 2019. Daytime rainy cloud detection and convective precipitation delineation based on a deep neural Network method using GOES-16 ABI images. Rem. Sens. 11 (21), 2555.
- Liu, Q., Xu, H., Sha, D., Lee, T., Duffy, D.Q., Walter, J., Yang, C., 2020. Hyperspectral infrared sounder cloud detection using deep neural network model. Geosci. Rem. Sens. Lett. IEEE 19 (2022), 5500705.
- Liu, Q., Chiu, L.S., Hao, X., Yang, C., 2021. Spatiotemporal trends and variations of the rainfall amount, intensity, and frequency in TRMM multi-satellite precipitation analysis (TMPA) data. Rem. Sens. 13 (22), 4629.
- McNally, A.P., Watts, P.D., 2003. A cloud detection algorithm for high-spectral-resolution infrared sounders. Q. J. R. Meteorol. Soc.: A j. atmos. sci. appl. meteorol. phys. oceanogr. 129 (595), 3411–3423.
- Mueller, B., Seneviratne, S.I., Jimenez, C., Corti, T., Hirschi, M., Balsamo, G., Ciais, P., Dirmeyer, P., Fisher, J.B., Guo, Z., Jung, M., 2011. Evaluation of global observations-based evapotranspiration datasets and IPCC AR4 simulations. Geophys. Res. Lett. 38 (6)
- Schlef, K.E., Moradkhani, H., Lall, U., 2019. Atmospheric circulation patterns associated with extreme United States floods identified via machine learning. Sci. Rep. 9 (1), 1–12
- Sekiguchi, M., Nakajima, T., Suzuki, K., Kawamoto, K., Higurashi, A., Rosenfeld, D., Sano, I., Mukai, S., 2003. A study of the direct and indirect effects of aerosols using global satellite data sets of aerosol and cloud parameters. J. Geophys. Res. 108 (D22), 4699.
- Sherwood, S.C., Wahrlich, R., 1999. Observed evolution of tropical deep convective events and their environment. Mon. Weather Rev. 127 (8), 1777–1795.
- Sikma, M., Vilà-Guerau de Arellano, J., 2019. Substantial reductions in cloud cover and moisture transport by dynamic plant responses. Geophys. Res. Lett. 46 (3), 1870–1878.
- Smith, J.A., Taylor, J.P., 2004. Initial cloud detection using the EOF components of high-spectral-resolution infrared sounder data. J. Appl. Meteorol. 43 (1), 196–210.
- Susskind, J., Barnet, C.D., Blaisdell, J.M., 2003. Retrieval of atmospheric and surface parameters from AIRS/AMSU/HSB data in the presence of clouds. IEEE Trans. Geosci. Rem. Sens. 41 (2), 390–409.
- Susskind, J., Barnet, C., Blaisdell, J., Iredell, L., Keita, F., Kouvaris, L., Molnar, G., Chahine, M., 2006. Accuracy of geophysical parameters derived from Atmospheric Infrared Sounder/Advanced Microwave Sounding Unit as a function of fractional cloud cover. J. Geophys. Res. Atmos. 111 (D9).
- Susskind, J., Blaisdell, J.M., Iredell, L., Keita, F., 2011. Improved temperature sounding and quality control methodology using AIRS/AMSU data: the AIRS science team version 5 retrieval algorithm. IEEE Trans. Geosci. Rem. Sens. 49 (3), 883–907.
- Susskind, J., Blaisdell, J.M., Iredell, L., 2014. Improved methodology for surface and atmospheric soundings, error estimates, and quality control procedures: the atmospheric infrared sounder science team version-6 retrieval algorithm. J. Appl. Remote Sens. 8 (1), 084994.
- Susskind, J., Kouvaris, L., Blaisdell, J.M., Iredell, L., 2017. Analysis of CrIS/ATMS using AIRS version-7 retrieval and QC methodology. December. In: AGU Fall Meeting Abstracts. A12B-05.
- Wang, L., Tremblay, D.A., Han, Y., Esplin, M., Hagan, D.E., Predina, J., Suwinski, L., Jin, X., Chen, Y., 2013. Geolocation assessment for CrlS sensor data records. J. Geophys. Res. Atmos. 118 (22), 12–690.
- Wang, P., Li, J., Li, J., Li, Z., Schmit, T.J., Bai, W., 2014. Advanced infrared sounder subpixel cloud detection with imagers and its impact on radiance assimilation in NWP. Geophys. Res. Lett. 41, 1773–1780.
- Wang, L., Chen, Y., Han, Y., 2016. Impacts of field of view configuration of Cross-track
 Infrared Sounder on clear-sky observations. Appl. Opt. 55 (25), 7113–7119.
 Wang, L., Zhang, B., Tremblay, D., Han, Y., 2017. Improved scheme for Cross-track
- Wang, L., Zhang, B., Tremblay, D., Han, Y., 2017. Improved scheme for Cross-track Infrared Sounder geolocation assessment and optimization. J. Geophys. Res. Atmos. 122 (1), 519–536.
- Wang, T., Luo, J., Liang, J., Wang, B., Tian, W., Chen, X., 2019. Comparisons of AGRI/ FY-4A cloud fraction and cloud top pressure with MODIS/Terra measurements over East Asia. J. Meteorol. Res. 33 (4), 705–719.
- Xu, H., Chen, Y., Wang, L., 2018. Cross-track infrared sounder spectral gap filling toward improving intercalibration uncertainties. IEEE Trans. Geosci. Rem. Sens. 57 (1), 509–519.
- Yang, C., Yu, M., Li, Y., Hu, F., Jiang, Y., Liu, Q., Sha, D., Xu, M., Gu, J., 2019. Big Earth data analytics: a survey. Big Earth Data 3 (2), 83–107.
- Zhou, Lihang, Divakarla, Murty, Liu, Xingpin, Layns, Arron, Goldberg, Mitch, 2019. An Overview of the Science Performances and Calibration/Validation of Joint Polar Satellite System Operational Products. Rem. Sens. 11, 698.
- Zou, C.Z., Zhou, L., Lin, L., Sun, N., Chen, Y., Flynn, L.E., Zhang, B., Cao, C., Iturbide-Sanchez, F., Beck, T., Yan, B., 2020. The reprocessed Suomi NPP satellite observations. Rem. Sens. 12 (18), 2891.